Microring Weight Banks

Alexander N. Tait, Allie X. Wu, Thomas Ferreira de Lima, Ellen Zhou, Bhavin J. Shastri, *Member, IEEE*, Mitchell A. Nahmias, and Paul R. Prucnal, *Fellow, IEEE*

***Abstract*—Microring weight banks could enable novel signal processing approaches in silicon photonics. We analyze factors limiting channel count in microring weight banks, which are central to analog wavelength-division multiplexed processing networks in silicon. We find that microring weight banks require a fundamentally different analysis compared to other wavelength-division multiplexing circuits (e.g., demultiplexers). By introducing a quantitative description of independent weighting, we establish performance tradeoffs between channel count and power penalty. This performance is significantly affected by coherent multiresonator interactions through bus waveguides. We experimentally demonstrate these effects in a fabricated device. Analysis relies on the development of a novel simulation technique combining parametric programming with generalized transmission theory. Experimental measurement fitting of an 8-channel weight bank is presented as an example of another application of the simulator.**

***Index Terms*—Microresonators, microwave photonics, neural network hardware, optical signal processing, photonic integrated circuits (PIC), silicon photonics.**

I. Introduction

COMMUNICATION bottlenecks in conventional computers and their incipient limitations have played a major role in motivating two major research thrusts: 1) silicon photonics manufacturing, in which the aim is to address the bandwidth and energy efficiency performance of these bottlenecks, and 2) unconventional computing architectures, in which the aim is to mitigate their limiting effect on processing. Silicon photonic device sets are designed for digital photonic links and are comprised of modulators [1], waveguides (WG), and detectors [2]. Wavelength-division multiplexing (WDM) is a common technique to channelize enormous usable optical bandwidth, so devices to (de)multiplex [3] and modulate [4] WDM signals are central to this effort. Analog optical interconnects have long been recognized for their potential to implement unconventional, distributed, and/or neuromorphic processing systems, wherein many simultaneous and continuously tunable connections are required. However, the enormous cost to develop scalable and/or integrated application-specific photonic signal processing platforms, in concert with rapid advances in digital signal processing technology, have posed practical barriers to past research in uconventional optical computing. Microring resonators (MRRs)—which are a common photonic circuit elements ubiquitous in WDM systems—could bring analog signal processing opportunities to silicon integrated photonic circuits. MRRs are easily created by bending a WG into a loop and offer the wavelength selectivity to perform tunable WDM functions [5].

Here, we introduce fundamental tools for quantitative analysis and engineering design of microring weight banks, including a simulation technique geared towards tunable devices and a new performance metric describing weight bank functional efficacy. Previously, it was reported that the maximum WDM channel count was approximately limited to 34 [6]; however, the rigorous modeling and metric analysis introduced in this paper indicates a limit near 108, given similar assumptions. This discrepancy can be partly attributed to the exploitation of coherent interactions between adjacent MRR filters, a measured physical effect that is not encompassed in conventional analyses of other WDM devices (e.g. demultiplexers). Other uses of the simulation approach are considered, and an example of experimental measurement fitting is presented. This work has direct implications for the limits of WDM analog network capacity in silicon and provides essential tools for designing advanced weight banks.

In analog and neural networks, connections between nodes or neurons are represented by real number weights [7], [8] that can be reconfigured on slow timescale. The system is programmed to perform a task by setting the weights of the network [9]. A number of modern neuromorphic architectures communicate with pulse-coded signals called spikes [10] to minimize energy consumption, and are amenable to event-based digital signaling and packet-routing techniques [11]. Packet-routing and time multiplexing have enabled the creation of large scale electronic neuromorphic cores but at the expense of harsh tradeoffs between scale and operational bandwidth [12]–[14].

Combining neural network models with photonics may yield a system capable of combining high operational bandwidth, scalable interconnect channelization, and low power distributed processing [15], [16]. Optical signals can have much greater bandwidths and lower crosstalk between multiplexed channels. Recent acceleration of high-performance, CMOS-compatible photonic integrated circuit (PIC) platforms promise to greatly expand the possibilities for large scale systems. An important component of current research efforts are foundry platforms that provide optimized fabrication and standardized device sets [17], [18]. Although these device sets are optimized for traditional, digital WDM communication links, they may also be repurposed for analog computation.

Manuscript received February 5, 2016; revised April 12, 2016; accepted May 16, 2016. This work was supported by the Defence Advanced Research Projects Agency Microtechnology Office under Grant MTO 4101916239 and the NSF Graduate Research Fellowship Program under Grant DGE 1148900.

The authors are with the Lightwave Communications Laboratory, Department of Electrical Engineering, Princeton University, Princeton, NJ 08544 USA (e-mail: atait@princeton.edu; axwu@princeton.edu; tlima@princeton.edu; ellenz@princeton.edu; shastri@ieee.org; mnahmias@princeton.edu; prucnal@princeton.edu).

Color versions of one or more of the figures in this paper are available online at http://ieeexplore.ieee.org.

Digital Object Identifier 10.1109/JSTQE.2016.2573583

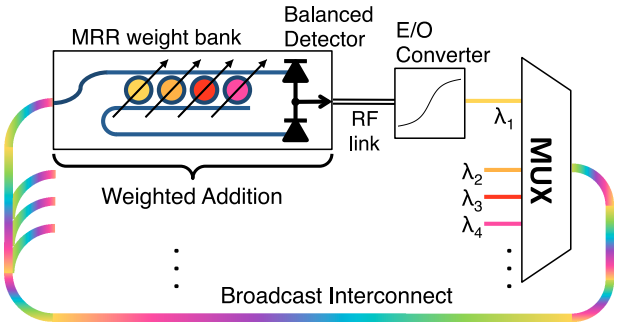

Fig. 1. Concept of an integrated broadcast-and-weight network [6]. An MRR weight bank provides the key functionality to configure connection strengths in the analog wavelength-multiplexed (WDM) network. Tuning each MRR between the on- and off-resonance states determines how much of a given WDM channel is split between 2 ports of balanced photodetector. The detected signal drives an electro-optic (E/O) converter, such as a laser, which generates a new optical signal at a unique wavelength.

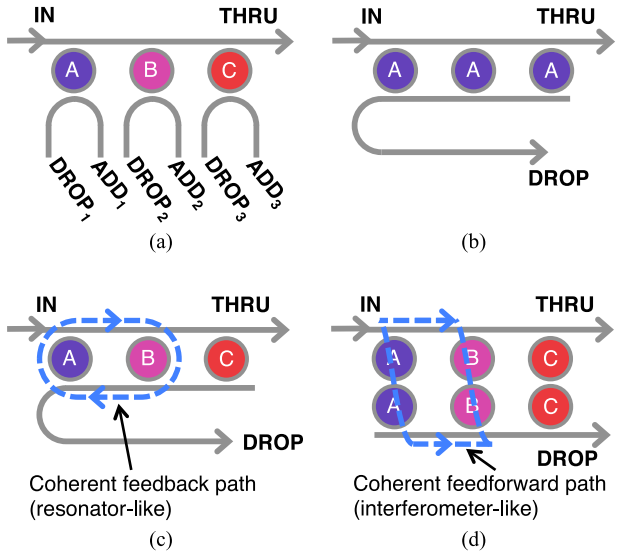

Fig. 2. (a) MRR optical add-drop multiplexer. Letters (A, B, and C) denote the WDM channel affected by a given MRR. Cross-talk occurs when a wavelength channel partially couples through a neighboring MRR, ending up at the incorrect DROP port. (b) MRR dual-channel SCISSOR. The SCISSOR has only one DROP port and one THRU port, and all resonators are nominally tuned to a single wavelength. (c) MRR weight bank with 1-pole (i.e. one MRR) filters. While there is only one DROP and THRU port, each MRR controls the weight of a distinct WDM channel. The presence of two bus WGs creates a path for coherent feedback between neighboring MRRs, which is resonator-like. (d) MRR weight bank with 2-pole filters. Because the signal does not change direction in the drop bus WG, multi-MRR coherent interactions manifest as feedforward (interferometer-like).

A silicon photonic architecture called "broadcast-and-weight" (see Fig. 1) was proposed as a way to interconnect photonic neurons on chip [6]. It is a wavelength-division multiplexed (WDM) protocol, similar to the broadcast-and-select protocol used in fiber ring networks [19], [20]. Instead of selecting WDM signals with an add/drop multiplexer, input signals are weighted by a tunable optical filter and then incoherently summed in a photodetector. As shown in Fig. 1, sets of MRRs can be collected on the input ports of each processor, allowing full reconfigurability of all N channels for each of N nodes in a broadcast network, totalling N^2 independent connections. MRR weight banks are the key photonic subcircuit associated with interconnection and network configuration in a broadcast-and-weight architecture. The scaling potential of analog networks in silicon are therefore closely tied to the performance limits of MRR weight banks, which must be better understood to allow the construction of larger networks.

MRRs are a natural choice to implement tunable weighted connections in silicon photonics. By tuning on and off resonance with an optical carrier signal, a MRR directs that signal to the through and drop ports, respectively, enabling complementary +/– weighting [21]. Continuous tuning along a single filter edge to effect a precise range of weights was shown in [22]. MRR weight banks consist of parallel-coupled microrings, each of which controls one of the WDM signals independently. A 4-channel MRR weight bank was demonstrated in [23]. Preliminary results on scaling analysis were presented in [24].

In this paper, we analyze factors limiting channel count in MRR weight banks and encounter a tradeoff between WDM channel spacing (a.k.a. density) and insertion loss. In conventional analyses of MRR devices for multiplexing, demultiplexing, and modulating WDM signals, the tradeoff that limits channel spacing is inter-channel cross-talk [25]–[27]. Analyses driven by cross-talk, however, are approximate when applied to weight banks. Unlike MRR demultiplexers where each channel is coupled to a distinct WG output [28], MRR weight banks have exactly two multiplexed outputs with some portion of every channel coupled to each. Since the outputs are still multiplexed when detected, the notion of cross-talk between signals breaks down. Any portion of a given channel coupled through the "wrong" MRR could be counter-balanced by reducing the coupling of its primary MRR, due to the continuously tunable nature of the device and its controller. Nevertheless, channel density limits do arise as neighboring filter peaks merge together and lose independent control over WDM channels. The metric introduced herein includes a notion of tuning range in order to quantify this degradation of independent weight control as an overall power penalty.

Weight banks have two parallel bus WG that are coupled to every MRR, a geometry that gives rise to coherent multi-resonator interactions not present in any other WDM device (see Fig. 2(a)). A channel partially coupled through a neighboring MRR—instead of causing inter-channel cross-talk—can return through the opposite bus WG to complete a coherent feedback path involving multiple MRRs (see Fig. 2(c)). As illustrated in Fig. 2(d), weight banks using even-pole MRR filters can also give rise to coherent feedforward paths that behave like interferometers. Multi-MRR coherent interactions are especially relevant when resonances are closely spaced, so it is essential to account for them in channel density analysis. At the same time, these interactions mean that a weight bank cannot be modeled as a simple composition of individual MRR models, thus motivating more involved simulations for entire weight bank devices. Coherent effects are found to have a significant impact on system behavior and scaling performance.

To the authors' knowledge, analysis of a two-bus device in which each MRR acts as a tunable filter for a distinct WDM

channel has not been performed. WG circuits of similar geometries have been used to tailor single-channel filtering aspects [29], including high-free spectral range (FSR) [30], [31] and flat passband [32]. Multi-resonator coherent effects have been analyzed [33], [34] and characterized [35] in double-channel side-coupled integrated spaced sequence of optical resonators (SCISSORs), although the resonant wavelengths of SCISSOR resonators are fixed and nominally identical (see Fig. 2(b)).

Section II will apply a generalized matrix transmission theory [36] suitable for describing coherent interactions. In Section IV, a simulation tool is introduced to efficiently model tunable WG circuits with coherent feedback, combining generalized transmission theory with parametric modeling and symbolic programming optimizations. Then, Section V-A defines a metric describing the efficacy of independent weighting in a multi-channel tunable optical weight bank, expressed in the form of a power penalty. Finally, Section V-B studies the system tradeoffs between power penalty and channel density and the impact of multi-MRR interactions on this tradeoff.

II. Theory

In this section, we begin with a brief mathematical description of how a generic tunable spectral filter with complementary outputs to a balanced photodetector can be formulated as a circuit for WDM weighted addition. Then, we derive expressions for transmission and weight values in a MRR implementation using the generalized transmission matrix theory developed in [36]. While a range of analytical modeling techniques have been successfully applied to microresonator circuits [37], [38], the continuously variable nature of weight banks necessitates generalized transmission modeling.

A. WDM Weighted Addition

A wavelength multiplexed signal consists of a set of N optical carriers with frequency, ω_i, whose power envelopes have been modulated to represent a set of N data signals, $x_i(t)$. If signal bandwidth is much less than the optical carrier frequency, a slowly-varying envelope approximation and short-time Fourier transform yield a convenient time-frequency expression for a WDM input:

$$E_{[\mathrm{in}]}(\omega,t)=\sum_{i=1}^{N}E_{0,i}\sqrt{1+x_i(t)}\delta(\omega-\omega_i) \tag{1}$$

where $E_{0,i}$ is the carrier field amplitude, δ is the Dirac delta function, and $x_i(t)$ is strictly greater than –1. This input signal is then sent into a tunable spectral filter, which is a linear optical system with both drop and through outputs. The transmission state of this filter is configured by tuning a parameter vector, $\vec{\Delta}$:

$$E_{[\mathrm{wei}]}^{(+,-)}(\omega,t)=H^{(+,-)}(\omega;\vec{\Delta})E_{[\mathrm{in}]}(\omega,t) \tag{2}$$

where H is a tunable spectral filter response with complementary outputs, indicated by +/– superscripts. Often the elements of $\vec{\Delta}$ represent resonant wavelength shifts, but they can also represent optical path lengths or absorptivity. Next the effect of a balanced photodiode (PD) is represented as the difference between two photocurrents derived from the weighted signals, which in turn are integrals over the wavelength domain of the still-multiplexed signals

$$i_{\mathrm{PD}}(t)=\int_{\omega}R(\omega)\left(\left|E_{[\mathrm{wei}]}^{+}(\omega,t)\right|^2-\left|E_{[\mathrm{wei}]}^{-}(\omega,t)\right|^2\right)d\omega \tag{3}$$

where $R(\omega)$ is detector responsivity. Compounding the effects of (1)–(3), we end up with a net function that fits the form of weighted addition, modulo a DC bias term

$$\mu_i=A_i\left(\left|H^{+}(\omega_i;\vec{\Delta})\right|^2-\left|H^{-}(\omega_i;\vec{\Delta})\right|^2\right) \tag{4}$$

$$y(t)=\sum_{i=1}^{N}\mu_i x_i(t)+\sum_{i=1}^{N}\mu_i \tag{5}$$

where $A_i\equiv R(\omega_i)\cdot Z_0/v_\pi\cdot E_{0,i}^2$ and $y=i_{PD}\cdot Z_0/v_\pi$ where v_π is the voltage at π phase shift and Z_0 is a characteristic impedance. This is the basic form of weighted addition: $y=\vec{\mu}\cdot\vec{x}$. We have made the assumption that the spacing between the ω_i's is significantly greater than the bandwidth of $x(t)$; otherwise, the summation could not be pulled out of the magnitude functions. In other words, coherent beat noise would corrupt the function of weighting. In further analyses, the A_i terms will be assumed identical between channels for simplicity. As seen in Eq. (4), the evaluation of weights μ_i depends on modeling the transmission functions $H^{(+,-)}$, which is now considered for MRR implementations of WDM weight banks.

B. Generalized Transmission Modeling

Fig. 3 illustrates a method for modeling the transfer function of a bank of MRRs with generalized 4-port transmission line couplers introduced in [36]. 4-ports can be composed into more general WG circuits through operations such as joining and port swapping, although this work focuses only on weight bank circuits. As shown in Fig. 3(a), a type-5 coupler with parameters (a,K_1), where a relates to the insertion loss parameter γ of the coupling as $a=\sqrt{1-\gamma}$, and K is the coupling coefficient, is used to model the coupling of a broadcast WG and a MRR. Then, the MRR itself (see Fig. 3(b)) can be modeled by a pair of transmission lines with lengths L_1, L_2, which meet in another type-5 coupler with parameters (a,K_2) connecting the ring and the drop WG. The combination of these plus a port swapping operation yield a type-3 coupler, illustrated in Fig. 3(c), that is used to model a single MRR with ports 1 and 3 attached to a broadcast WG and ports 2 and 4 to a drop WG (see Fig. 3(d)). Bus WGs connecting MRR filters have lengths ΔL_{BW} and ΔL_{DW}. While instructive, a derivation of the scattering and transfer matrices of a single MRR is deferred for brevity. An interested reader can refer to this derivation in Appendix VII.

The main result of the single MRR derivation can be expressed as the amplitude transmission of the MRR through (T_j)

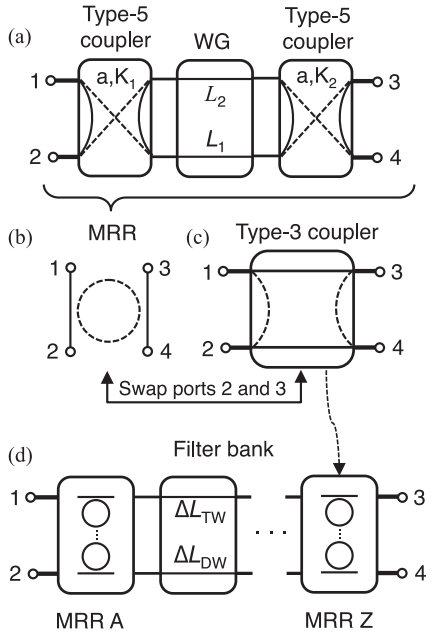

Fig. 3. (a) Model construction of a MRR weight bank following method shown in ref. [36]. WG and optical couplers are modeled as 4-port transmission line coupler blocks. In these couplers, solid and dashed lines represent a direct and a coupled connection, respectively. a relates to the insertion loss parameter γ of the coupling as $a = \sqrt{1-\gamma}$, and K is the coupling coefficient. WG blocks only have direct connections with a phase shift proportional to the optical path length (nL). (b) An MRR can be modeled with two couplers modeling the WG-ring interactions and a WG block modeling each arm of the ring. (c) Then, these blocks are joined to form a MRR filter, which is effectively a type-3 coupler, i.e. one with a direct connection between opposite ports and coupled connection between ports on the same side. Note that this coupler is no longer symmetrical because of different K- and L-values. (d) MRR Filters can be joined together by WG blocks to form a weight bank. BW refers to broadcast WG and DW to drop WG.

and drop (D_j) ports:

$$T_j = \underbrace{a\sqrt{1-K_j}}_{\text{indirectcoupling}} \cdot \underbrace{(1-FK_j)}_{\text{neg.res.feedback}} \tag{6}$$

$$\begin{aligned} D_j = & \underbrace{ai\sqrt{K_1}}_{\text{couplingtop}} \cdot \underbrace{ai\sqrt{K_2}}_{\text{couplingbottom}} \cdot \underbrace{e^{-(\alpha+i\beta)l_j}}_{\text{opticalpath}} \\ & \cdot \underbrace{F}_{\text{pos.res.feedback}} \\ = & -a^2\sqrt{K_1K_2}e^{-(\alpha+i\beta)l_j}F \end{aligned} \tag{7}$$

where the cavity-resonance amplification factor $F \triangleq [1 - G\exp(-i\beta L)]^{-1}$, βL is the round-trip phase shift, and $\beta = 2\pi n_{\text{eff}}/\lambda = n_{\text{eff}}\omega/c$ is the wavenumber of the WG. Eq. (6) can be intuitively understood as follows: the amplitude of the incoming signal drops by $a\sqrt{1-K_j}$ because of the insertion loss of the coupling between the MRR and the broadcast WG; part of the signal gets coupled to the MRR with amplitude drop of $i\sqrt{K_j}$; however, the coupled signal completes the loop around the MRR and comes back to the broadcast-MRR junction with an amplitude of F and couples back onto the broadcast loop with another amplitude drop of $i\sqrt{K_j}$; the feedback signal then interferes with the transmitted one, yielding an interference factor of $1 + i\sqrt{K_j}\cdot F \cdot i\sqrt{K_j} = (1 - FK_j)$. Since F is maximum when the MRR is on resonance, the MRR effectively induces a negative resonance feedback.

Eq. (7) can be read with the same intuition: the incoming signal couples in and out of the rings with amplitude drops of $i\sqrt{K_1}$ and $i\sqrt{K_2}$ (the order is unimportant since the factors multiply); moreover, the optical path induces a loss of $e^{-\alpha l_j}$ and a phase shift of $e^{-i\beta l_j}$; at the junction of the MRR and the drop WG, the same round trip interference mechanism present in 7 takes place, but without signals coming from the ADD port, the interference term is simply F. In this case, the dropped signal is maximized when F is maximum—i.e. when the MRR is on resonance—so the MRR effectively induces a positive resonance feedback. Note: the effect of the ring resonance is entirely contained in the variable F, and it is precisely the factor that allows the dropped signal to have significant amplitude despite small coupling factors $\sqrt{K_j}$.

1) 2-Channel Weight Bank: The scattering transfer matrix of multiple 4-port couplers can be multiplied in cascade to yield the scattering matrix of the MRR bank. The S-matrix in eq. (15) can be transformed back into an equivalent A-matrix (eq. (8)) [36]:

$$A_{\text{MRR}} = \begin{bmatrix} \frac{1}{T_1} & 0 & 0 & -D_2T_1^{-1} \\ 0 & \frac{T_1T_2 - D_1D_2}{T_2} & D_1T_2^{-1} & 0 \\ 0 & -D_2T_2^{-1} & T_2^{-1} & 0 \\ \frac{D_1}{T_1} & 0 & 0 & \frac{T_1T_2 - D_1D_2}{T_1} \end{bmatrix}. \tag{8}$$

Let us denote the lengths of the bus WGs connecting two neighboring rings on the through side and on the drop side as ΔL_{TW} and ΔL_{DW}, respectively. The A-matrix for this component reads:

$$A_{\text{WG}} = \text{diag}\left(e^{j\theta_{\text{TW}}}, e^{-j\theta_{\text{TW}}}, e^{j\theta_{\text{DW}}}, e^{-j\theta_{\text{DW}}}\right)$$

where $\theta_{\text{TW,DW}} = (\beta - i\alpha)\Delta L_{\text{TW,DW}}$. Let us define $\Delta L \triangleq \Delta L_{\text{TW},+\Delta\text{LDW}}$. We will index the two rings as MRR A and MRR B, but we will assume that the two rings have the same coefficients a and $K_{1,2}$. The total scattering transfer matrix can be computed as:

$$A_{\text{2MRR}} = A_{\text{MRR,A}} \cdot A_{\text{WG}} \cdot A_{\text{MRR,B}}$$

which can be readily converted to an S-matrix. Due to symmetry, we are only interested in the elements S_{31} (THRU) and S_{21} (DROP). In this situation, it can be shown that:

$$S_{31}(\text{2MRR}) = T_{1,A}T_{1,B}e^{-\Delta L_{\text{TW}}(\alpha+i\beta)}F_{\text{AB}} \tag{9}$$

$$S_{21}(\text{2MRR}) = D_{1,A} + T_{1,A}D_{1,B}T_{2,A}e^{-\Delta L(\alpha+i\beta)}F_{\text{AB}} \tag{10}$$

where a convenient factor $F_{AB} = [1 - D_{1,B}D_{2,A}e^{-\Delta L(\alpha+i\beta)}]^{-1}$ is introduced. Inspecting F_{AB}, one can realize that it is a converged sum of an infinite geometric series of factor $D_{1,B}D_{2,A}e^{-\Delta L(\alpha+i\beta)}$, which is the complex attenuation factor of the round trip between the two rings: $D_{1,B}$ is the drop factor at ring B, $D_{2,A}$ is the drop factor at

ring A from its ADD port and $e^{-\Delta L(\alpha+i\beta)}$ is the attenuation due to the WGs connecting the two rings. While the analytical approach yields intuitive insight in the 2-filter case, higher order expressions are unwieldy for the scope of this work (refer to Appendix VII). Fig. 3(a) diagrams the process of joining waveguides and couplers into an MRR filter, which are then joined into a weight bank structure (see Fig. 3(d)). A computationally efficient implementation of this construction is discussed in Section IV.

It is worth noting that neglecting the resonant feedback effect between MRRs is equivalent to removing F_{AB} from the expressions. This *incoherent approximation* is valid when MRR resonant frequencies are spaced far apart because either $D_{1,B}$ or $D_{2,A}$ is very small at every given wavelength. This is not the case when the resonators are densely spaced in the wavelength domain, which is exactly the case of interest for analyzing channel density limits. Due to the centrality of this physical effect to this work, as well as its absence from other WDM devices to which channel density is also meaningful, we perform an experimental investigation of coherent interactions using a specialized MRR weight bank.

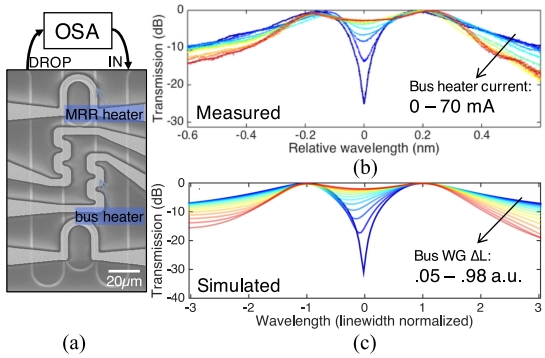

Fig. 4. Experimental verification of coherent weight interaction within a 2-channel weight bank with bus tuning heaters. (a) SEM of device under test. An OSA measures the transmission between the bank's IN port and DROP port. (b) Measured response of the device as bus heater current is applied equally to both bus heaters. MRRs are tuned until separated by 0.4 nm (2 linewidths). Then bus current is varied over 0–70 mA such that heater power is sampled uniformly. Thermal cross-talk causes the resonances to shift absolutely, but their spacing stays consistent. Absolute wavelength shifts of the central minimum between peaks have been removed. (c) Simulated response of this device when resonances are spaced by 2 linewidths and bus WG phase is swept over a half period, 0–π, which corresponds to slightly less than 1.0 arbitrary length units in this simulation.

III. Experimental Validation

The resonant feedback interaction between MRRs depends coherently on the optical path length of the bus WGs. In order to study how the phase condition of the bus affects multi-MRR interaction, we fabricate a 2-channel silicon weight bank with tunable bus WGs. This experimentally verifies that this physical effect is significant for MRR weight banks. Observations are fit using the parameterized simulator introduced in Section IV to validate model accuracy. The results suggest intuitively that coherent interactions in bus WGs could play a significant role in WDM channel density analysis, which is formalized in Section V.

A. Methods

Samples were fabricated on silicon-on-insulator wafers at the Washington Nanofabrication Fabrication through the UBC SiEPIC fabless rapid prototyping group [39]. Silicon thickness is 220 nm, and buried oxide thickness is 3 μm. 500 nm wide WGs were patterned by Ebeam lithography and fully etched to the buried oxide [40]. A hydrogen silsesquioxane resist (HSQ, Dow-Corning XP-1541-006) was spin-coated at 4000 rpm, then hotplate baked at 80 °C for 4 minutes. Electron beam lithography was performed using a JEOL JBX-6300FS system operated at 100 keV energy, 8 nA beam current, 500 μm exposure field size, and exposure dose of 2800 μC/cm^2. The resist was developed by immersion in 25% tetramethylammonium hydroxide (TMAH) for 4 minutes. Silicon was etched from unexposed areas by inductively coupled plasma etching in an Oxford Plasmalab System, with a chlorine gas flow of 20 sccm, pressure of 12 mT, ICP power of 800 W, bias power of 40 W, and a plate temperature of 20 °C, resulting in a bias voltage of 185 V.

Ti-Pt-Au heating contacts (100Å:Ti, 2000Å:Au) were then deposited on top of a 3 μm oxide passivation layer using an Angstron Engineering electron beam evaporation system. Ohmic heating in these contacts causes thermo-optic index shifts, so that a heater patterned on top of a MRR can tune its resonant wavelength. Heater power is controlled by a 13-bit digital-to-analog converter (DAC), NI PCI-6723, which is buffered to provide up to 80 mA per channel. The sample is mounted on a temperature-controlled alignment stage. The TE WG mode is coupled from the silicon circuit to a fiber array using focusing subwavelength grating coupler arrays [41]. An optical transmission spectrum analyzer (OSA) measures the transfer functions from IN to DROP ports and from IN to THRU ports.

B. Tuning Coherent Interaction With Bus Heaters

The weight bank used to test coherent interactions between MRR weights consists of two racetrack resonators with perimeters of 80.0 and 80.1 μm parallel-coupled to two bus WGs (see Fig. 4(a)). Individual Q-factors are 7750. Resonances are thermally tuned by ohmic heating in metal contacts. Additional heaters are patterned over each bus WG, which are 60 μm long. To test this device, we first used the MRR heaters to adjust two resonances to a 0.4 nm separation ($\sim$2 filter linewidths). We then tuned bus heaters nonuniformly between 0 and 70 mA, such that the data traces were taken at intervals approximately uniform in electrical heater power.

Current is applied equally to each bus heater to prevent creating an asymmetric temperature profile across the device. The heaters' meandering shape is intended to localize heat as much as possible, but thermal cross-talk is still present, causing changes in bus current to shift filter resonances. By applying current equally and relying on the (rough) symmetry of the device, both resonators are made to shift together, maintaining their spacing at 2 linewidths. Background shifts are removed in Fig. 4(b). Differences in phase between bus WGs would be difficult to study with this technique, but are not expected to have an impact on resonator-like coherent interaction effects.

Fig. 4(b) shows that bus tuning significantly affects the dip between filters, whose depth ranges from -2.7 dB to -25.0 dB relative to peak transmission. The steepness of rolloff regions are also slightly affected. The measurements closely match corresponding simulations in which the effective bus phases were parameterized and swept uniformly, shown in Fig. 4(c). This verifies that the parametric simulator can make accurate predictions about weight banks in the dense channel regime. While the device layout is symmetric, the asymmetry observable in the spectra of Fig. 4(b) and (c) can be explained by the fact that inputs encounter the MRRs in a particular order.

From an intuitive standpoint, it seems that this coherent effect that depends on bus phase could have a significant impact on channel density. If the goal is to be able to set the weight/transmission of neighboring WDM channels independently, then it would be disadvantageous to have the responses blur into a single peak like the red traces in Fig. 4(b) and (c). On the other hand, it may be possible to take advantage of the deep isolation between peaks represented by the blue traces. Bus tuning elements could prove useful in large scale MRR weight banks because they provide full control over multi-MRR effects, which may be otherwise difficult to control in the presence of fabrication variance and thermal cross-talk. In Section V, we will quantify the degree to which weights can be set independently and use the simulator to study how this metric is affected by channel spacing and MRR interaction. An approach for efficient simulation of tunable MRR devices with multiple coherent paths is now discussed in more detail.

IV. Parameterized Simulator

Parameterized modeling is a powerful tool for engineering analysis, particularly for tunable systems. While a numerical simulation can predict the response of a particular device in a particular state, a parameterized model is a function of free parameters or can be thought of as a representation of all the possible states of a particular device. Combined with different search and optimization functions, parameterized models are at the heart of problems such as finding a state that reproduces an observed response (e.g. measurement fitting), finding a state that gives a desired response (e.g. optimization, feedforward control), or performing analyses in reference to a *range* of possible states, such as the weight states (see Section V-A).

Pre-computation is an important consideration in the implementation of parameterized models. Pre-computing every possible response rapidly becomes intensive, as the number of states needed to sample the entire range grows exponentially with the number of parameter dimensions. A more fruitful approach involves separating the overall model into sub-systems that have a fixed or otherwise invariant response. These sub-responses may be reused when a parameter is changed. For example, in the case of the MRR demultiplexer in Fig. 2(a), upon tuning the downstream MRR-C, we would know that the DROP_1 output cannot change, thus saving new computation. In addition, linear system theory provides an obvious way to break the MRRs into completely independent transmission responses, which are then simply multiplied to obtain the overall response. Although tuning the upstream MRR-A may affect the DROP_3 output, it does not affect the transmission response of MRR-C, thus saving some recomputation.

Separating the MRR weight bank into sub-systems is more challenging because of the potential for feedback along the bus WGs (see Fig. 2(b)). Feedback necessitates the generalized matrix transfer method, which introduces significant algebraic interdependence and complexity. This means that, in principle, any parameter change could affect the signal at every point in the device. On the other hand, the algebraic outcome of generalized matrix analysis must contain some structure—for example, tuning a heater would not change the number of rings—so it seems that some amount of pre-computation would be possible, if the structure of dependencies could be automatically identified. Many languages provide symbolic math packages that are well suited for automating analytic manipulations and their numeric evaluations.

By combining symbolic programming methods with generalized matrix transfer theory, we obtain an efficient parametric simulator for WG circuits. Circuit values, such as a WG length, are represented as symbolic variables within the S-matrices of low-level components. The transfer matrices of two 4-port components can be composed to yield another 4-port [36], allowing the construction of successively more complex general circuits. This construction is illustrated for a MRR weight bank in Fig. 3. Before connecting filters of one or more MRR into a bank structure, ports 2 and 3 must be swapped. The final symbolic object representing the entire filter bank retains the symbolic nature of the low-level values (i. e. λ, a, K etc.). The symbolic expression is easy to manipulate but not efficient at evaluating numeric values. It is converted into a function optimized for numerics using a built-in package function.

Finally, the optimized functions for S_{31} and S_{21} are wrapped in a parametric model object, which also contains WDM channel frequencies and an array of parameters. Parameters have specifiable default and free range properties. Simple model functions through, drop, and weight feed parameter defaults to $|S_{31}|^2$, $|S_{21}|^2$, and $|S_{31}|^2 - |S_{21}|^2$, respectively. Other functions determine internally which parameters to use within the range. The metric defined in Section V-A is currently implemented by a simple sweeper, but other functions for optimizing, controlling, or fitting measurements for devices described by a generalized transmission model could be incorporated into this interface.

A. Measurement Fitting Example

Measurement fitting is an important capability for studying devices experimentally. Fitting consists of calculating the error between observed data and the predictions of a model. The state space of the model is searched in order to minimize the error in its prediction. This allows the recovery of underlying physical values based on observation. In the case of models with many parameters, searching the high dimensional parameter space can involve many evaluations of the model, so this is a key area where speedup has an impact. We take spectral transmission measurements of an 8-channel weight bank and

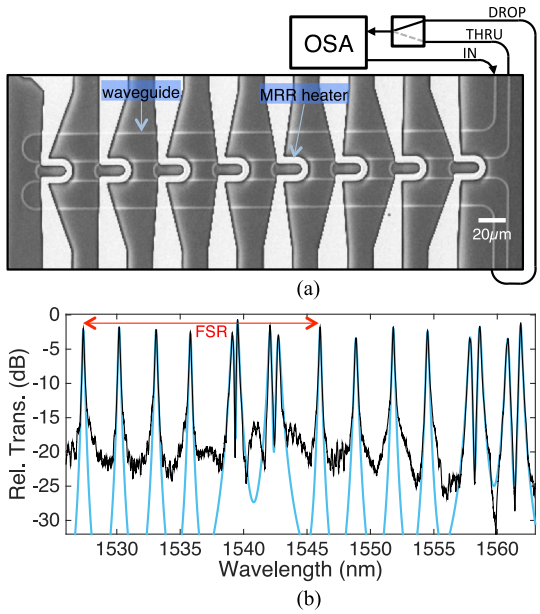

Fig. 5. Measurement fitting of an 8-channel MRR weight bank. (a) SEM image: 8 racetrack resonators are parallel coupled to two bus WGs and can be thermally tuned by gold heating elements. An OSA is connected to either drop or through port. (b) The measured transmission spectrum of drop port (black line) compared to the parametric fit (blue line). The blue fit spectrum a single contiguous curve, despite leaving the window. The depth of experimental data is limited by an amplifier noise floor around –20dB. The FSR of a single resonator is indicated in red. Two resonances of each MRR are pictured.

use the presented simulation approach to accurately fit this data. We find that using a pre-computed symbolic model results in an evaluation speedup of more than 2000×.

An 8-channel weight bank shown in Fig. 5(a) was fabricated and measured with experimental methods as described in Section III. The racetrack resonators in the measured device have perimeters of $[30.0, 30.1, \ldots, 30.7]\mu$m, and all directional coupling gaps between bus and MRR WGs are 200 nm wide with a 2 μm long straight section[1]. Both drop and through spectra are measured and plotted over two FSR periods in Fig. 5(b) (black line). The 8 sets of resonances are roughly evenly spaced, although no thermal tuning is applied. A single filter has a measured FSR of 18.7 nm and Q-factor of 11 070. That means their finesse is 133, which is an important figure for determining the WDM channel count that would be possible using resonators of this design.

A parametric transmission model of an 8-MRR weight bank was created and fit to the measured spectra using a nonlinear optimization algorithm. The effective optical perimeters of the 8 resonators, all 16 directional coupling coefficients, 7 bus WG optical path lengths, and global WG loss are represented symbolically during the pre-computation phase. These parameters are composed using the generalized transmission matrix theory, and the resulting expression is computationally optimized by the MATLAB symbolic engine. The model thus provides a total of 32 parameter dimensions. To improve performance, the program neglected interaction between non-neighboring MRRs. Where possible, the program also neglects parameters that have a small effect, such as the bus length between neighbors with sufficiently distant resonance wavelengths. The general decomposition of large models with strong coherent effects into synthesized nearest-neighbor models represents an area for further research. To ensure convergence to the correct minimum, an initial guess of the resonance wavelengths is provided by picking peak wavelengths present in the measured spectrum. During each iteration of the optimizer, a trial parameter vector is used to simulate a single drop transmission spectrum. The root mean squared error between the model response and measured data is used as an objective score of that particular trial parameter vector. A Nelder-Mead simplex search successively updates the trial parameters in order to minimize the objective function.

The result of the model after fitting is shown in Fig. 5(b) (blue line). The model successfully reproduces the important features of the experimental spectrum. In particular, the accuracy of the model in reproducing dips between densely spaced resonances indicate the need for coherent modeling of the bus WGs to capture multi-MRR effects. This is most apparent in the resonances due to MRRs 5 and 6 and the resonances due to MRRs 7 and 8 (counting the lowest wavelength resonance at ∼1527.3 nm as MRR 1). The noise floor feature of the optical spectrum analyzer occuring around –20 dB is not captured by this model.

The computational performance of the symbolic parametric modeling technique was assessed through comparison with a fully numeric modeling baseline. The symbolic 8-MRR model takes 3.3 minutes to pre-compute and 6.7 μs to evaluate a single transmission point on a laptop CPU with 16GB of RAM. A fully numeric evaluation of a particular tuning state was made by substituting in numeric parameter values and a numeric array of wavelength points into the transmission model builder. The numeric model requires no pre-computation, but takes 13.7 ms per transmission point to evaluate. This means the symbolic pre-computation approach can accelerate evaluation by a factor of over 2000×; however, the program structure was originally designed for algebraic constructions and the numeric speed could likely improve with appropriate optimization. While not necessary in all applications, there are many cases where a large number of evaluations of different parameter states are necessary. In this measurement fitting example, approximately 4300 calls were made to the modeling function during the optimization phase. Rapid evaluation is extremely important for high-accuracy fitting of high-resolution measurements of complex devices with reasonable convergence time. It is also important for studying aspects of multi-dimensional tuning *ranges*, as employed in the following section.

V. Channel Scaling Analysis

An important question regarding any multichannel system is the number of channels that can be supported. Analyzing this problem usually involves identifying a limiting effect that causes

[1]We note that the design of the measured device differs slightly from that of the pictured device, which has racetrack perimeters of $[60.0, 60.1, \ldots, 60.7]\mu$m and straight coupling sections that are 10 μm long.

degradation of some performance metric as the number of channels increases. Specifying a worst-case allowable performance results in a channel limit.

In conventional analyses of MRR devices for multiplexing, demultiplexing, and modulating WDM signals, the limiting metric that degrades with channel spacing is cross-talk between channels [25]–[27]. Cross-talk occurs when a WDM signal couples through a neighboring filter, appearing effectively as noise to an unintended photodetector. In [26], a potential maximum WDM channel count of 62 was simulated under the specification of cross-talk isolation $>$20 dB.

In [6], an incoherent analysis was applied to weight banks by incorporating the resonance tuning aspect, resulting in 34 channels. This analysis was limited in several regards. Firstly, the acceptable level of cross-talk isolation was chosen somewhat arbitrarily, since there is little data on its role in analog networks. Secondly, even the definition of cross-talk in a weight bank was not properly considered because all of the WDM channels are detected in the same photodetectors, regardless of which path they take through the weight bank. Finally, coherent effects in the bus were neglected, although we find here that they play a key role when weight bank channels are dense.

A. Cross-Weight Power Penalty Metric

The notion of inter-channel cross-talk is not a meaningful concept in MRR weight banks. This presents a problem for channel scaling analysis since previous analytical methods use inter-channel cross-talk as the driving metric that degrades with channel count. Furthermore, coherent interactions between multiple MRRs in a weight bank make metrics based on isolated add-drop filters because the bank response must be treated as that of a single transmission element with several degrees of freedom. A new metric that accounts for these unique features is called for. We introduce a metric called cross-weight power penalty that quantifies the ability of a real WDM weight bank to independently control signals as compared to an ideal WDM weight bank.

In the single-channel case, an ideal tunable weight bank possesses a range of tuning states that include directing an incident optical signal completely to a through port (positive weight), completely to a drop port (negative weight), or to any intermediate ratio of both. If a real weight incurs some loss, its weight range becomes a subset of the ideal. Supposing there is a difference in loss between the drop and through ports, then the attainable weight range will also be unbalanced. It is fair to assume that in the majority of cases where weights are used, they are required to be balanced such that, by some normalization factor they can effect a range of weights from –1 to +1. We can then define the usable range of the single-channel weight as the zero-centered interval whose span is determined by the minimum absolute value of the extreme positive weight and the extreme negative weight. Comparing the usable range to the ideal range yields a ratio, W, that quantifies the real device's ability to perform tunable optical weighting

$$W = \min\left[\max_{p}(\mu), \max_{p}(-\mu)\right] \tag{11}$$

where p is the tuning parameter and μ is the weight. At this point, it should be noted that this balanced normalization factor relies on the concept of the extrema of a weight *range*. While it is often obvious, in general, we do not know which states in the tuning parameter space correspond to these weight extrema prior to sweeping, searching, or otherwise optimizing.

Since weighting is a linear function, the normalization factor between ideal and usable ranges is conveniently stated as a power penalty, meaning the additional optical input power needed to reproduce the power level that would be present with an ideal device. Power penalty is a useful tool for quantitative system analysis because it allows comparison of disparate effects. Single-channel examples of effects that can all be associated with a power penalty include a responsivity mismatch in the balanced PD, in-ring propagation loss disproportionately affecting dropped signals, and, of course, bus propagation loss affecting all signals. A multi-channel power penalty metric is needed to study the effect of multi-MRR interaction and—most importantly for this analysis—channel spacing.

In the N-channel case, the ideal WDM weight bank is able to switch WDM channels completely independently from one another. It can be thought of as a set of N isolated, ideal single-channel weights; however, the N-channel generalization of a non-ideal weight bank is more complex. If a given tuning parameter can affect multiple weight values, then the bank's weight range cannot be linearly separated into any composition of non-ideal single-channel weight ranges. Fig. 6 depicts this mapping for a simulated 2-channel bank that is parameterized by the MRR detunings. Channel spacing is 1.31 linewidths, and WG loss is 2dB/cm. The tuning range (see Fig. 6(a)) is constrained to best represent a realistic N-channel case, such that 0 refers to on-resonance and 1 refers to one channel spacing. While the 2-channel weight range could be expanded by detuning in opposite directions or by detuning by many channel spacings, neither strategy is possible with more channels.

A uniform 2-D sweep over tuning range results in an irregular distribution of points in 2-D weight space (see Fig. 6(b)). To visualize the correspondence between tuning and weights, a (red, blue) color vector is assigned to each weight point to indicate the corresponding tuning vector: (detuning 1, detuning 2) $= (\Delta\omega_1/\delta\omega, \Delta\omega_2/\delta\omega) = \Delta\vec{\omega}/\delta\omega$. As in the 1-D case, a usable range can be defined as the largest balanced interval (i.e. a zero-centered square in 2-D) that is completely covered by the attainable weight range. The usable range (green square in Fig. 6(b)) is compared to the theoretical ideal (black bounding box in Fig. 6(b)). The ratio of their side lengths, W_x, represents the non-idealities associated with multi-channel weighting (W_x =0.45 in this example). This ratio is referred to as the cross-weight power penalty and can be stated in decibels as $-10\log(W_x)$, or 3.5 dB in this example.

Fig. 6(c) shows the simulated drop port transmission spectra at the 4 extrema of the parameter sweep. A (red, blue) coloring of traces indicates correspondence with the tuning vector. The (0, 0)-detuning resonance condition (pure black) has two peaks centered at zero and one channel spacing where channels 1 and 2 are respectively located. (0, 1)-detuning (pure blue) has the deepest dip at the channel 2 center frequency. (1, 1)-detuning

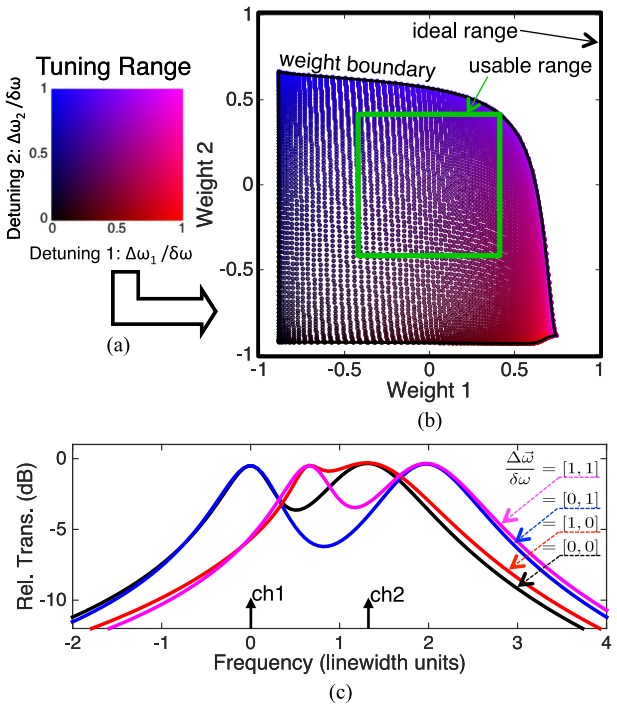

Fig. 6. Example of cross-weight power penalty in a 2-channel MRR weight bank. (a) The device has two tuning degrees-of-freedom, which are resonance detunings of each filter. A (red, blue) color vector is used to indicate tuning state, which means that (a) depicts (red=x, blue=y). (b) The range of possible weight states attainable by the weight bank relative to the ideal range (outer bounding box). (red,blue) color indicates the tuning state which maps to a particular weight point. The usable range (green box) is graphically the largest square that lies fully within the possible weight range centered at zero. (c) Drop port spectra of the same model over a 5 × 5 parameter grid, with trace color used to indicate tuning. Frequency is normalized so that the MRR 1 peak has a center of 0 and FWHM of 1.0. Channel spacing in this simulation is 1.31 linewidths.

(magenta) is very similar to (0, 0)-detuning, but shifted relative to the channels. (1, 0)-detuning (pure red) appears almost as a single peak centered on channel 2. The (1, 0)-detuning state is highly sensitive to coherent effects similar to electromagnetically-induced transparency, in which the dip width can be much narrower than the peak width. This sensitivity can be seen as a small abnormality and densification of points (i.e. sharp color changes) around the corresponding red region in Fig. 6(b). If some WG loss is not included in the model, this region can also become sensitive to numerical instabilities.

Cross-weight penalty can be formulated in more precise terms. The point cloud in Fig. 6(b) is actually a sampling of a continuous and smooth manifold. The tuning range is a Cartesian parameterization of this weight manifold, with a mapping described by the transmission theory (see Section II). Since its parameterization is bounded, the weight manifold must also have a well-defined boundary. In 2D, that boundary is a simple closed curve (black outline in Fig. 6(b)) meaning that this boundary, $\boldsymbol{B} \in \mathcal{R}^2$, can be parameterized by a circle:

$$\boldsymbol{B}(s) = [\mu_1(s), \mu_2(s)] \qquad 0 < s < 2\pi \tag{12}$$

where μ_i is the channel i weight.

We estimate this boundary curve from the discrete point cloud using a conforming boundary algorithm [42], [43]. The conforming boundary is unlike the convex hull in that it can shrink inwards to better estimate a continuous manifold sampled by discrete points, provided the samples are sufficiently dense. On the curve $\boldsymbol{B}$, there is a single point that limits the usable tuning range, W_x, which is found as

$$W_x = \min_s \left[\max_{i=1,2} |\mu_i(s)| \right] \tag{13}$$

where the absolute value ensures +/– balance and the inner maximum over channels ensures equal ranges between channels. Graphically, W_x is the size of the largest square that intersects the boundary $\boldsymbol{B}$. This definition of cross-weight penalty as the intersection of a manifold boundary with a zero-centered interval can extend to arbitrary numbers of N channels by replacing s with a vector $\vec{s}$ that parameterizes an $N-1$ dimensional boundary of the N dimensional range of states. We focus on the 2-channel case henceforth.

B. Loss-Density Tradeoff

The final step of channel density analysis is to study the degradation of the limiting metric as WDM channel spacing becomes more dense. A useful figure of merit for discussing the efficacy of a resonator-based circuit at a WDM task is the ratio of finesse to channel count. This figure is the same as the linewidth-normalized channel spacing and somewhat independent of the type or performance of the resonator platform. The theoretical minimum of this figure is 1.0 for amplitude modulated signals, at which point the signals themselves mutually interfere. Simulations are performed in linewidth units so that a discussion of finesse and resonator implementations can be deferred until the end.

The 2-channel weight bank model described in the previous section is modified so that its system operating points (channel spacing, $\delta\omega$, and bus length changes, ΔL) are variable. A 50 × 50 sweep over operating points is then performed. $\delta\omega$ ranges from 0 to 9 linewidths, and ΔL ranges from 0 to 0.2 in units relative to the initial bus length. The length of both bus WGs are held equal to one another. For each operating point in this sweep, the usable weight range and cross-weight power penalty are calculated from a 300 × 300 point sweep over MRR detunings constrained between 0 and 1 channel spacing, as described in the previous section. At a given operating point, the cross-weight algorithm holds $\delta\omega$ and ΔL constant, treating them as fixed system parameters. The 50 × 50 sweep over 300 × 300 tuning points and 2 channel frequencies, comprising 450M evaluations of Eqs. (9) and (10), is completed in roughly 5 minutes due to the optimizations described in Section IV.

Fig. 7(a) shows the resulting power penalty contours of $-10\log(W_x)$ vs. $\delta\omega$ and ΔL. We can make several conclusions from this plot. Firstly, the power penalty has an asymptote as channel spacing hits a wall. As the filter peaks merge together, all frequencies are coupled to the drop port, making it impossible to reach a weight of (0, 0). This means there is an absolute minimum channel spacing, regardless of acceptable

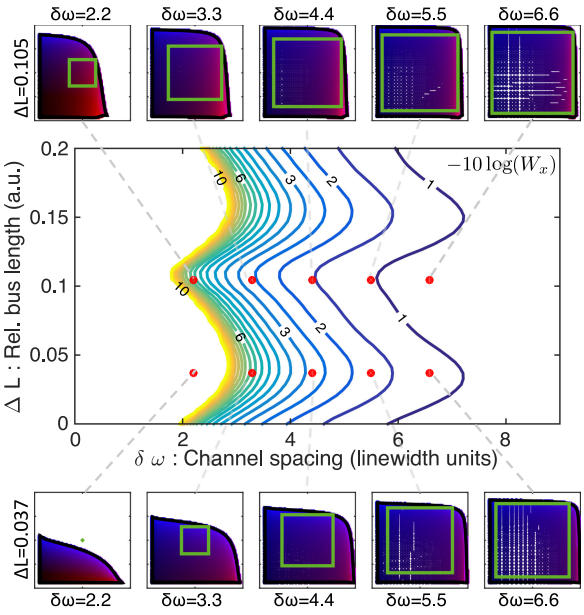

Fig. 7. Cross-weight power penalty surface as a function of channel spacing $\delta\omega$ and bus WG length offset ΔL. Power penalty contours are plotted at 0.5 dB increments between 1 dB (blue) and 10 dB (yellow). The penalty increases as channel density decreases, eventually reaching an asymptote. This tradeoff also depends significantly and approximately periodically on ΔL, indicating the influence of coherent multi-MRR interactions in the bus WGs. (outer panels) Ranges of possible weight states, plotted as in Fig. 6(b), at 10 selected operating points that are indicated in (a) by red circles. The top row, $\Delta L = 0.105$, represents the best-case tradeoff between power and channel density, and the bottom row, $\Delta L = 0.037$, represents the worst-case.

power penalty. The displayed 10 dB contour (yellow) is very close to this asymptote.

Secondly, the cross-weight power penalty decreases smoothly as channel spacing is increased above the absolute cutoff. This represents a system design tradeoff between WDM channel spacing and power penalty. The maximum channel count can be determined based on the power budget allowed for weighting, or the excess power requirement can be set by a given channel specification. The power penalty cannot quite reach 0 dB because of optical losses.

Thirdly, both the channel density wall and the tradeoff between density and loss are significantly affected by bus length changes. The resulting approximate periodicity (here, ∼0.12 in arbitrary length units) is indicative of a coherent effect, which can be expected based on the possibility of resonator-like multi-MRR interactions when resonances are at similar frequencies. Examining the 10 dB contour, the channel spacing wall fluctuates with ΔL between 0.85 and 1.4 linewidths. What is perhaps surprising is that the effect of bus length remains significant even when channels are spaced relatively far apart. The 3 dB contour line fluctuates between 3.41 and 4.61 linewidths over a period of ΔL.

Fig. 7(b) depicts attainable weight ranges at 5 channel spacings and the best- and worst-case bus lengths. Plot format is as described in Fig. 6(b), and 10 dots in Fig. 7(a) indicate the channel spacing and bus length corresponding to each plot. This offers further information about some of the mechanisms behind the performance trends. With decreasing channel spacing, the usable range (green) is impacted both by an overall smaller area covered by the possible weight range, but also an increased warping of this range away from square. From row to row, one sees that the top always performs better. The best and worst cases for ΔL do not depend on $\delta\omega$. The bottom-leftmost panel shows an example of an nonviable weight range that does not cover (0,0).

C. Channel Scaling Limits

The limits of channel count in WDM devices implemented by resonators is the number of channels that can fit within one FSR. Channel count is closely related to the finesse of the resonator, defined as the ratio of FSR and the resonator linewidth (i.e. full-width half-maximum (FWHM)). It can be thought of as a theoretical maximum on channel count for a given resonator design. On the other hand, real devices cannot reach this limit due to performance degradation of interchannel cross-talk or, in this case, cross-weight power penalty. Channel count, N, is therefore also related to the ratio of WDM channel spacing to filter linewidth as

$$N \leq \frac{\mathcal{F}}{\delta\omega} \tag{14}$$

where $\mathcal{F}$ is finesse, and $\delta\omega$ is the linewidth-normalized channel spacing. This equation conveniently separates effects impacting channel count since $\mathcal{F}$ pertains only to resonator properties, while $\delta\omega$ describes circuit behavior independent of resonator type.

Making an assumption that a 3 dB cross-weight penalty is allowed, Fig. 7 indicates that the minimum channel spacing falls between 3.41 and 4.61 linewidths depending on bus length. A corresponding figure can be calculated for cross-talk driven demultiplexer analyses at 2.5 in [27] and 5.8 in [25] whose discrepancy can be attributed to different choices of cross-talk specification. In [6], a cross-talk driven analysis was applied to tunable MRR weight banks, estimating a channel spacing of 8.8: nearly double the worst-case estimate obtained in this work. Channel spacing could be driven closer to 1.0 with circuit techniques such as multi-pole filters consisting of serial-coupled resonators. The analytical approach introduced in this work enables future quantitative design of advanced weight bank circuits for increasing channel density.

A finesse of 133 was observed in the 8-channel silicon weight bank tested in Fig. 5. This yields absolute channel count of 39 for this type of resonator, although it was not optimized for finesse. Optimized MRR design, such as demonstrated in [44] (finesse = 368) and [45] (finesse = 540), could potentially support 108 and 148 channels, respectively, in a MRR weight bank circuit. Other types of resonators in silicon, such as elliptical microdisks [46] (finesse = 440) and traveling-wave microresonators [47] (finesse = 1,140) could potentially reach up to 129 and 334 channels, respectively. Demultiplexers have been demonstrated with 20 channels in [3], [48], and with up to 32 channels in [49]. In practice, control and fabrication issues complicate the demonstration of large WDM devices; however, this is also a key area of development for mainstream digital

communications in silicon photonics [50], [51] and therefore can be expected to improve.

The footprint of the filters needed for a network can be estimated from the channel count and resonator size. Supposing we use the resonator from [44] (channel count = 108), then the approximate footprint of a single filter bank in this case is 108 $\times$ 5 μm $\times$ 5 μm=2700 μm^2. The corresponding N-to-N network footprint is $108 \times 2700 = 0.29$ mm^2. We have made the simplifying assumptions that every connection has a dedicated tunable MRR filter, these filters are all critically coupled to the bus WG, and that they are single-pole (i.e. single-MRR).

VI. Discussion

While the rigorous numeric result for channel number is important, the analytical method and tools developed in this paper raise many more questions and directions for quantitative design. A MRR weight bank is in many ways appears similar to a MRR add/drop demultiplexer, with the slight difference that it does not actually demultiplex. This difference in behavior necessitates a novel channel density analysis based on cross-weight penalty instead of inter-channel cross-talk. It also creates the possibility of resonant modes involving multiple MRRs and bus WGs.

The optical length of the bus has a substantial effect on performance, so we would like to understand how to account for it. It is unlikely that this length can be controlled lithography due to fabrication variations, similar to the problem of exactly hitting a MRR resonance [52]. A larger issue when thermal tuning is used for weighting is thermal cross-talk because the effective bus length will change even if there is not a tuning element upon it. A limitation of the analysis put forth was that thermal cross-talk was neglected, and it could have an impact on the data in Fig. 7. A study such as this could be performed by symbolically setting the value of the four WG lengths to linear combinations of two tuning parameters.

Fabricating real bus tuning elements (as in Fig. 4(a)) would provide a means to bias bus phases post-fabrication, although it adds to the number of tuning ports and DAC channels required per weight. This leads to another interesting possibility where there are more heater tuning dimensions than weight dimensions, which can only serve to increase the span of the possible weight range. In this type of analysis, a 4-dimensional tuning range would map onto a 2-dimensional weight range, after which, it is the same analysis. A practical issue of this scheme is that 4-dimensional sweeps can contain many more points that need to be evaluated.

Multi-pole filters consisting of series-coupled MRRs can be used in WDM systems for steeper rolloff resulting in denser channel spacing [53] or to increase the finesse [54]. Most interesting in the case of a MRR weight bank is that the nature of coherent interactions will be fundamentally affected by the filter order parity because the direction of the drop port is reversed. With odd-parity filter banks, resonant feedback loops are possible; whereas the even-parity banks have no possibility of feedback, and instead may exhibit properties more reminiscent of Mach-Zehnder interferometers. Whether or not this is advantageous is a design question to which our performance analysis could be applied. While the cross-weight penalty metric running with a fast parametric transmission simulator (see Section IV) will be a useful design tool for MRR weight banks, we expect that there could be other applications of the simulator to other types of tunable WG circuits.

Some of the unique requirements of a MRR weight bank make feedback weight control a challenge, but feedforward control has been shown [23]. Model-based strategies become essential for controlling multi-channel MRR weight banks once inter-channel dependencies are introduced. In past work, the optical weight bank itself was operated in a regime in which filters did not interact and therefore did not require optical modeling. As channels become more dense, the practical problem of control must involve transmission models of weight banks that have two kinds of parameters: unknown device parameters, which are fit based on measurement and then fixed, and heater tuning dependent parameters. Fitting parameters for thermal cross-talk from measurements is relatively trivial compared to fitting a transmission model, so the parametric simulator will likely play a role in scalable control approaches for MRR weight banks.

VII. Conclusion

We derived performance limits of MRR weight banks, finding that an allowed 3 dB power penalty resulted in a minimum channel spacing between 3.41 and 4.61 linewidths. This tradeoff depends coherently on the optical path length of bus WGs. More generally, we developed analytical methods and simulation tools for MRR weight banks, which serve to establish a foundation for system design.

MRR weight banks are unique amongst WDM devices in that MRRs controlling different channels are all parallel-coupled to the same bus WGs. Inter-channel cross-talk is ill defined in this case, so a new metric was introduced to quantify ability to weight channels independently over a complete tuning. The cross-weight power penalty exhibits a direct tradeoff with channel density, leading to performance limits. Channel power coupling through incorrect MRRs creates the possibility of resonances involving multiple MRRs and bus WGs. This effect was experimentally validated and found to have a significant impact on device performance. The combination of a metric defined in regards to a range of possible states along with a model with coherent feedback presents a modeling challenge for which an efficient simulator based on symbolic parameterization was introduced. This simulation technique could possibly find use in fitting, control, or design problems for MRR weight banks or other silicon WG circuits. In tying together ideas from multi-wavelength networking and analog signal processing, microring weight banks could unlock brand new domains of computing based on silicon photonics.

Appendix: Single MRR Transmission

A derivation of a single MRR scattering and transfer matrix is included for instruction in this appendix. The derivation results in the analytic expression of microring drop and through transmissions in Eqs. (6) and (7). One can calculate the scattering

transfer matrix A_{MRR} which relates the left-hand side inputs (1:IN and 2:DROP) to the right-hand side outputs (3:THRU and 4:ADD) as such:

$$\begin{bmatrix} a_1 & b_1 & a_2 & b_2 \end{bmatrix}^T = A_{\mathrm{MRR}} \begin{bmatrix} b_3 & a_3 & b_4 & a_4 \end{bmatrix}^T$$

where a_i and b_i represent signals coming respectively into and out of port i as in ref. [36]. This is useful because the scattering transfer matrix multiple MRRs is the product of the individual scattering transfer matrices. Another possible representation of a 4-port coupler is the scattering matrix S_{MRR}, which gives the relationship between outcoming signals and incoming signals to all ports:

$$\begin{bmatrix} b_1 & b_2 & b_3 & b_4 \end{bmatrix}^T = S_{\mathrm{MRR}} \begin{bmatrix} a_1 & a_2 & a_3 & a_4 \end{bmatrix}^T.$$

The relationship between S_{MRR} and A_{MRR} can be easily derived and is explicitly shown in ref. [36]. The S matrix for a single MRR using a type-3 coupler (see Fig. 3(b)) design described above should have the form:

$$S_{\mathrm{MRR}} = \begin{bmatrix} 0 & D_1 & T_1 & 0 \\ D_1 & 0 & 0 & T_2 \\ T_1 & 0 & 0 & D_2 \\ 0 & T_2 & D_2 & 0 \end{bmatrix} \tag{15}$$

where we introduced the parameters $D_{1,2}$ and $T_{1,2}$ to highlight the symmetry of the system: e.g. if the input is in port 1, the transmission (S_{31}) and drop (S_{21}) coefficients are T_1 and D_1, respectively. Note that we have ignored here backscattering terms ($S_{11} = S_{41} = 0$). The asymmetry between T_1 and T_2 is explained by the different coupling coefficients K_1 and K_2 and that of D_1 and D_2 is explained by the possible different path lengths of each arm of the microring. These distinctions will soon be mathematically clear. This matrix was explicitly calculated in ref. [55]. However, the analysis of a weight bank filter will require an intuitive way of expressing each term T_j and D_j, because multiple rings will interfere with each other in interesting ways. First, we define a set of helpful variables: the round-trip amplitude loss of the microring cavity as $G \triangleq a^2\sqrt{1-K_1}\sqrt{1-K_2}\exp(-\alpha L)$, where $L = L_1 + L_2$ is the cavity length (see Fig. 3(a)); and the cavity-resonance amplification factor $F \triangleq [1 - G\exp(-i\beta L)]^{-1}$, where βL is the round-trip phase shift and $\beta = 2\pi n_{\mathrm{eff}}/\lambda = n_{\mathrm{eff}}\omega/c$ is the wavenumber of the WG. Obs. 1: Note that since $G < 1$, F is maximized when the phase shift is an integer multiple of 2π, i.e. when the microring is on resonance. Obs. 2: F is the converged sum of the infinite geometric series of factor $G\exp(-i\beta L)$, which is the round-trip complex amplitude loss of the ring.

Appendix: N-Channel Weight Bank

A generalized analysis for periodically distributed sequence of microrings indirectly coupled to two common WGs was previously studied—dubbed double-channel SCISSOR (side-coupled integrated spaced sequence of resonators) [33]. The study showed that the distributed resonant feedback created photonic band gaps in either WG irrespective of the loss parameter a for matched coupling coefficients (K_1 and K_2 picked in such a way that $(1 - K_j F) = 0$ (see Eq.(6)).

Because the optical path lengths between microrings can be tuned, our analysis has to be more general to take these into account. In filter banks with a large sequence of MRRs, coherent interference due to the resonance of three or more rings also take effect, yielding extra resonance factors such as F_{AC}, F_{BD} etc. Thankfully there is an intuitive way to compute and to analytically express these terms. First, let us define a few useful sets:

1) $\Omega_{\mathrm{left}}(\Theta,\Lambda) = \{(\Theta_1,\Lambda)\}$ such that $\Theta \le \Theta_1 < \Lambda$. E.g. $\Omega_{\mathrm{left}}(B,E)$ is equal to $\{(B,E),(C,E),(D,E)\}$
2) $\Omega_{\mathrm{right}}(\Theta,\Lambda) = \{(\Theta,\Theta_2)\}$ such that $\Theta < \Theta_2 \le \Lambda$. E.g. $\Omega_{\mathrm{right}}(B,E)$ is equal to $\{(B,C),(B,D),(B,E)\}$
3) $\Omega_{\mathrm{all}}(\Theta,\Lambda) = \{(\Theta_1,\Theta_2)\}$ such that $\Theta \le \Theta_1 < \Theta_2 \le \Lambda$. E.g. $\Omega_{\mathrm{all}}(B,E)$ is equal to $\{(B,C),(C,D),(D,E),(B,D),(C,E),(B,E)\}$

These sets are useful because it allows us to select, for example, all *super-rings*, i.e. an ordered pair of rings, contained between ring A and ring D ($\Omega_{\mathrm{all}}(A,D)$). All these rings are going to have a resonant feedback effect in the transmitted power. Equipped with these definitions, and naming MRRs from A to $\mathrm{L}(n)$ (the n-th letter in latin alphabet), the analytical form of the terms S_{31} and S_{21} in (14) and (15), where $d_{\Lambda,\Theta}$ is the distance between letters Λ and Θ

$$S_{31}(n\text{−rings}) = e^{-(n-1)\Delta L_{\mathrm{TW}}(\alpha+i\beta)} \cdot \prod_{\Theta=A}^{\mathrm{L}(n)} T_{1,\Theta} \cdot \prod_{(\Theta_1,\Theta_2)\in\Omega_{\mathrm{all}}(A,\mathrm{L}(n))} F_{\Theta_1\Theta_2} \tag{14}$$

$$S_{21}(n\text{−rings}) = \sum_{m=1}^{m=n} D_{1,\mathrm{L}(m)} e^{-(m-1)\Delta L(\alpha+i\beta)} \cdot \left(\prod_{\Lambda=A}^{\mathrm{L}(m)-1} T_{1,\Lambda} T_{2,\Lambda} \prod_{(\Theta_1,\Theta_2)\in\Omega_{\mathrm{right}}(\Lambda,\mathrm{L}(n))} F_{\Theta_1\Theta_2} \right) \tag{15}$$

with

$$F^{-1}_{\Theta\Lambda} = 1 - D_{1,\Lambda} D_{2,\Theta} e^{-d_{\Lambda,\Theta}\Delta L(\alpha+i\beta)} \cdot \left(\prod_{\Gamma=\Theta+1}^{\Lambda-1} T_{1,\Gamma} T_{2,\Gamma} \right) \cdot \left(\prod_{(\Theta_1,\Theta_2)\in\Omega_{\mathrm{all}}(\Theta,\Lambda-1)} F_{\Theta_1\Theta_2} \right) \cdot \left(\prod_{(\Theta_1,\Theta_2)\in\Omega_{\mathrm{all}}(\Theta+1,\Lambda)} F_{\Theta_1\Theta_2} \right) \tag{16}$$

Despite the intimidating look of (14), it has recognizable terms: a complex amplitude loss term $e^{-L(\alpha+i\beta)}$, a product of transmittivity value for each ring Θ $T_{1,\Theta}$ and a product of all resonant feedback terms F. Equation (15) is more complicated, but still has identifiable terms. The electric field amplitude at the drop port is the coherent sum of all the dropped signals in

every ring, which explains the summing term $\sum_{m=1}^{m=n} D_{1,\mathrm{L}(m)}$. Each interfering term at the drop port of A, however, is amplified by the resonant feedback of pairs of rings formed by A and another ring to the *right* of A. Equation (16) is more complicated to understand, but it was derived and analytically verified by symbolic calculation of the $S_3 1$ and $S_2 1$ originating from cascaded scattering transfer matrix multiplication employed in Section II-B1.

The interest of the analytical expressions (14) and (15) is that it allows for smart approximation of scattering terms for a great number of MRRs ($n \gg 1$): one could, for example, neglect all resonant feedback and only consider microring resonances ($F_{AB} = FBC = \cdots = 1$), or one could neglect resonant feedback of more than three rings ($F_{AC} = FBD = \cdots = 1$), making the analysis more tractable. We hope that these analytical expressions will help optimize the design of large filter banks taking into account coherent interference.

ACKNOWLEDGMENT

Fabrication support was provided via the Natural Sciences and Engineering Research Council of Canada Silicon Electronic-Photonic Integrated Circuits Program. Devices were fabricated by Richard Bojko at the University of Washington Washington Nanofabrication Facility, part of the NSF National Nanotechnology Infrastructure Network.

REFERENCES

[1] G. T. Reed, G. Mashanovich, F. Y. Gardes, and D. J. Thomson, "Silicon optical modulators," *Nature Photonics*, vol. 4, no. 8, pp. 518–526, 2010.

[2] L. Vivien *et al.*, "42 GHz p.i.n germanium photodetector integrated in a silicon-on-insulator waveguide," *Opt. Express*, vol. 17, no. 8, pp. 6252–6257, Apr. 2009.

[3] M. S. Dahlem *et al.*, "Reconfigurable multi-channel second-order silicon microring-resonator filterbanks for on-chip WDM systems," *Opt. Express*, vol. 19, no. 1, pp. 306–316, Jan. 2011.

[4] S. Manipatruni, L. Chen, and M. Lipson, "Ultra high bandwidth WDM using silicon microring modulators," *Opt. Express*, vol. 18, no. 16, pp. 16 858–16 867, Aug. 2010.

[5] S. Feng *et al.*, "Silicon photonics: from a microresonator perspective," *Laser Photonics Rev.*, vol. 6, no. 2, pp. 145–177, 2012.

[6] A. N. Tait, M. A. Nahmias, B. J. Shastri, and P. R. Prucnal, "Broadcast and weight: An integrated network for scalable photonic spike processing," *J. Lightw. Technol.*, vol. 32, no. 21, pp. 3427–3439, Nov. 2014.

[7] G. Indiveri *et al.*, "Neuromorphic silicon neuron circuits," *Front. Neurosci.*, vol. 5, no. 73, 2011.

[8] P. A. Merolla *et al.*, "A million spiking-neuron integrated circuit with a scalable communication network and interface," *Science*, vol. 345, no. 6197, pp. 668–673, 2014.

[9] A. Mundy, J. Knight, T. Stewart, and S. Furber, "An efficient SpiNNaker implementation of the neural engineering framework," in *Proc. Int. Joint Conf. Neural Netw.*, Jul. 2015, pp. 1–8.

[10] J. Misra and I. Saha, "Artificial neural networks in hardware: A survey of two decades of progress," *Neurocomputing*, vol. 74, no. 1/3, pp. 239–255, 2010.

[11] S. Furber *et al.* "Overview of the SpiNNaker system architecture," *IEEE Trans. Comput.*, vol. 62, no. 12, pp. 2454–2467, Dec. 2013.

[12] B. Benjamin *et al.* "Neurogrid: A mixed-analog-digital multichip system for large-scale neural simulations," *Proc. IEEE*, vol. 102, no. 5, pp. 699–716, May 2014.

[13] F. Akopyan *et al.* "TrueNorth: Design and tool flow of a 65 mW 1 million neuron programmable neurosynaptic chip," *IEEE Trans. Comput.-Aided Design Integr. Circuits Syst.*, vol. 34, no. 10, pp. 1537–1557, Oct. 2015.

[14] G. Indiveri and S.-C. Liu, "Memory and information processing in neuromorphic systems," arXiv:1506.03264, 2015.

[15] M. A. Nahmias, B. J. Shastri, A. N. Tait, and P. R. Prucnal, "A leaky integrate-and-fire laser neuron for ultrafast cognitive computing," *IEEE J. Sel. Topics Quantum Electron.*, vol. 19, no. 5, Sep./Oct. 2013, Art. no. 1800212.

[16] B. J. Shastri *et al.*, "Spike processing with a graphene excitable laser," *Sci. Rep.*, vol. 5, Dec. 2015, Art. no. 19126.

[17] A.-J. Lim *et al.* "Review of silicon photonics foundry efforts," *IEEE J. Sel. Topics Quantum Electron.*, vol. 20, no. 4, pp. 405–416, Jul. 2014.

[18] J. S. Orcutt *et al.*, "Open foundry platform for high-performance electronic-photonic integration," *Opt. Express*, vol. 20, no. 11, pp. 12222–12232, May. 2012.

[19] R. Ramaswami, "Multiwavelength lightwave networks for computer communication," *IEEE Commun. Mag.*, vol. 31, no. 2, pp. 78–88, Feb. 1993.

[20] X. Zhang, J. Wei, and C. Qiao, "Constrained multicast routing in WDM networks with sparse light splitting," *J. Lightw. Technol.*, vol. 18, no. 12, pp. 1917–1927, Dec. 2000.

[21] A. Tait *et al.*, "Balanced WDM weight banks for analog optical processing and networking in silicon," in *Proc. IEEE/OSA Summer Topicals Meeting Ser.*, Jul. 2015, pp. 110–111.

[22] A. Tait, T. F. de Lima, M. Nahmias, B. Shastri, and P. Prucnal, "Continuous calibration of microring weights for analog optical networks," *IEEE Photon. Technol. Lett.*, vol. 28, no. 8, pp. 887–890, Apr. 2016.

[23] A. N. Tait, T. F. de Lima, M. A. Nahmias, B. J. Shastri, and P. R. Prucnal, "Multi-channel control for microring weight banks," *Opt. Express*, vol. 24, no. 8, pp. 8895–8906, Apr. 2016.

[24] A. Wu *et al.*, "Coherent interactions in microring weight banks and impact on channel density," in *Proc. IEEE Opt. Interconnects Conf.*, May. 2016, pp. 50–51.

[25] K. Preston, N. Sherwood-Droz, J. Levy, and M. Lipson, "Performance guidelines for WDM interconnects based on silicon microring resonators," in *Proc. Conf. Lasers Electro-Opt.*, May. 2011, pp. 1–2.

[26] N. Sherwood-Droz, K. Preston, J. S. Levy, and M. Lipson, "Device guidelines for WDM interconnects using silicon microring resonators," in *Proc. Workshop Interaction Between Nanophoton. Devices Syst.*, 2010, vol. 43, pp. 15–18.

[27] H. Jayatilleka *et al.*, "Crosstalk in SOI microring resonator-based filters," *J. Lightw. Technol.*, vol. PP, no. 99, pp. 1–1, 2015.

[28] E. Klein *et al.*, "Reconfigurable optical add-drop multiplexer using microring resonators," *IEEE Photon. Technol. Lett.*, vol. 17, no. 11, pp. 2358–2360, Nov. 2005.

[29] O. Schwelb, "Phase-matched lossy microring resonator add/drop multiplexers," *Proc SPIE*, vol. 6343, pp. 63433P-1–63433P-10, 2006.

[30] R. Grover *et al.*, "Parallel-cascaded semiconductor microring resonators for high-order and wide-FSR filters," *J. Lightw. Technol.*, vol. 20, no. 5, p. 900–905, 2002.

[31] D. Geuzebroek *et al.*, "Thermally tuneable, wide FSR switch based on micro-ring resonators," presented at the Annual Symp. IEEE/LEOS Benelux Chapter, Vrije Universiteit Amsterdam, Amsterdam, The Netherlands, 2002.

[32] A. Melloni, "Synthesis of a parallel-coupled ring-resonator filter," *Opt. Lett.*, vol. 26, no. 12, pp. 917–919, Jun. 2001.

[33] J. E. Heebner, P. Chak, S. Pereira, J. E. Sipe, and R. W. Boyd, "Distributed and localized feedback in microresonator sequences for linear and nonlinear optics," *J. Opt. Soc. Amer. B*, vol. 21, no. 10, pp. 1818–1832, Oct. 2004.

[34] O. Schwelb, "Microring resonator based photonic circuits: analysis and design," in *Proc. IEEE Int. Conf. Telecommun. Modern Satellite, Cable Broadcasting Services*, 2007, pp. 187–194.

[35] M. Mancinelli *et al.*, "Optical characterization of a SCISSOR device," *Opt. Express*, vol. 19, no. 14, pp. 13 664–13 674, Jul. 2011.

[36] O. Schwelb, "Generalized analysis for a class of linear interferometric networks. I. Analysis," *IEEE Trans. Microw. Theory Techn.*, vol. 46, no. 10, pp. 1399–1408, Oct. 1998.

[37] C. J. Kaalund and G.-D. Peng, "Pole-zero diagram approach to the design of ring resonator-based filters for photonic applications," *J. Lightw. Technol.*, vol. 22, no. 6, pp. 1548–1559, Jun. 2004.

[38] M. T. Wade and M. A. Popović, "Efficient wavelength multiplexers based on asymmetric response filters," *Opt. Express*, vol. 21, no. 9, pp. 10903–10916, May. 2013.

[39] L. Chrostowski and M. Hochberg, *Silicon Photonics Design: From Devices to Systems*. Cambridge, U.K.: Cambridge Univ. Press, 2015.

[40] R. J. Bojko *et al.*, "Electron beam lithography writing strategies for low loss, high confinement silicon optical waveguides," *J. Vac. Sci. Technol., B, Microelectron. Process. Phenom.*, vol. 29, no. 6, 2011.

[41] Y. Wang *et al.*, "Focusing sub-wavelength grating couplers with low back reflections for rapid prototyping of silicon photonic circuits," *Opt. Express*, vol. 22, no. 17, pp. 20652–20662, 2014.
[42] A. A. Goshtasby, "Parametric circles and spheres," *Comput. Aided Design*, vol. 35, no. 5, pp. 487–494, Apr. 2003.
[43] B. Gao, S.-G. Hu, X.-W. Song, and X.-l. Yu, "Theory of constructing closed parametric curves based on manifolds," *Frontiers Elect. Electron. Eng. China*, vol. 1, no. 4, pp. 451–454, 2006.
[44] Q. Xu, D. Fattal, and R. G. Beausoleil, "Silicon microring resonators with 1.5-μm radius," *Opt. Express*, vol. 16, no. 6, pp. 4309–4315, 2008.
[45] A. Biberman, M. J. Shaw, E. Timurdogan, J. B. Wright, and M. R. Watts, "Ultralow-loss silicon ring resonators," *Opt. Lett.*, vol. 37, no. 20, pp. 4236–4238, Oct. 2012.
[46] K. Xiong *et al.*, "Single-mode silicon-on-insulator elliptical microdisk resonators with high Q factors," in *Proc. Photon. Optolectron. Meetings*, 2011, vol. 8333, pp. 83330A-1–83330A-7.
[47] M. Soltani, Q. Li, S. Yegnanarayanan, and A. Adibi, "Toward ultimate miniaturization of high Q silicon traveling-wave microresonators," *Opt. Express*, vol. 18, no. 19, pp. 19541–19557, Sep. 2010.
[48] C. W. Holzwarth *et al.*, "Fabrication strategies for filter banks based on microring resonators," *J. Vac. Sci. Technol., B, Microelectron. Process. Phenom.*, vol. 26, no. 6, pp. 2164–2167, 2008.
[49] S. Park, K.-J. Kim, I.-G. Kim, and G. Kim, "Si micro-ring MUX/DeMUX WDM filters," *Opt. Express*, vol. 19, no. 14, pp. 13531–13539, Jul. 2011.
[50] J. A. Cox, A. L. Lentine, D. C. Trotter, and A. L. Starbuck, "Control of integrated micro-resonator wavelength via balanced homodyne locking," *Opt. Express*, vol. 22, no. 9, pp. 11279–11289, May. 2014.
[51] H. Jayatilleka *et al.*, "Wavelength tuning and stabilization of microring-based filters using silicon in-resonator photoconductive heaters," *Opt. Express*, vol. 23, no. 19, pp. 25084–25097, Sep. 2015.
[52] L. Chrostowski *et al.*, "Impact of fabrication non-uniformity on chip-scale silicon photonic integrated circuits," in *Proc. Opt. Fiber Commun. Conf. Exhib.*, 2014, pp. 1–3.
[53] J. C. C. Mak *et al.* "Automatic resonance alignment of high-order microring filters," *IEEE J. Quantum Electron.*, vol. 51, no. 11, pp. 1–11, Nov. 2015.
[54] P. Saeung and P. P. Yupapin, "Vernier effect of multiple-ring resonator filters modeling by a graphical approach," *Opt. Eng.*, vol. 46, no. 7, 2007, Art. no. 075005.
[55] O. Schwelb, "Transmission, group delay, and dispersion in single-ring optical resonators and add/drop filters—A tutorial overview," *J. Lightw. Technol.*, vol. 22, no. 5, pp. 1380–1394, May. 2004.

Authors' photographs and biographies not available at the time of publication.